



# *In situ* derived Ni<sub>2</sub>P/Ni encapsulated in carbon/g-C<sub>3</sub>N<sub>4</sub> hybrids from metal–organic frameworks/g-C<sub>3</sub>N<sub>4</sub> for efficient photocatalytic hydrogen evolution



Jixiang Xu, Yinhong Qi, Lei Wang\*

Key Laboratory of Eco-Chemical Engineering, Taishan Scholar Advantage and Characteristic Discipline Team of Eco Chemical Process and Technology, College of Chemistry and Molecular Engineering, Qingdao University of Science and Technology, Qingdao, 266042, China

## ARTICLE INFO

### Keywords:

g-C<sub>3</sub>N<sub>4</sub>  
Ni-MOF-derived  
Ni<sub>2</sub>P/Ni  
Carbon materials  
H<sub>2</sub> evolution

## ABSTRACT

Tightly coupling multiple cocatalysts into semiconductors for efficient charge separation is a promising way to enhance photocatalytic H<sub>2</sub> production. In this work, Ni<sub>2</sub>P/Ni nanoparticles (NPs) encapsulated in carbon/g-C<sub>3</sub>N<sub>4</sub> hybrids derived from *in situ* pyrolysis and phosphidation of Ni-based metal–organic frameworks/g-C<sub>3</sub>N<sub>4</sub> (Ni-MOF/g-C<sub>3</sub>N<sub>4</sub>) precursor were used as photocatalysts for H<sub>2</sub>-evolution under visible-light irradiation. The highest H<sub>2</sub>-evolution rate over optimized Ni<sub>2</sub>P/Ni@C/g-C<sub>3</sub>N<sub>4</sub>-550 was 18.04 mmol g<sup>-1</sup> h<sup>-1</sup> with 1.0 mmol L<sup>-1</sup> of Eosin Y (EY)-sensitization (compared to 0.21 mmol g<sup>-1</sup> h<sup>-1</sup> without EY-sensitization), 13 times higher than that of pristine g-C<sub>3</sub>N<sub>4</sub> (1.33 mmol g<sup>-1</sup> h<sup>-1</sup>). The apparent quantum efficiency at 420 nm was 58.1%. This enhanced photocatalytic activity can be attributed to an efficient and rapid separation of the photo-generated charges from excited EY and g-C<sub>3</sub>N<sub>4</sub> to Ni<sub>2</sub>P/Ni with carbon as an electron transport bridge, intimate contact of each components, staggered band alignment among g-C<sub>3</sub>N<sub>4</sub>, Ni and Ni<sub>2</sub>P, as well as accelerated proton reduction reaction by Ni<sub>2</sub>P/Ni NPs. This work provides new insights into the construction of MOFs-derived cocatalyst for photocatalytic H<sub>2</sub> production.

## 1. Introduction

Utilizing solar light to irradiate photocatalysts/water system to generate H<sub>2</sub> is a promising route for easing energy crisis and global environmental contamination issues [1–5]. One of the key challenges for the application of photocatalytic H<sub>2</sub> evolution is the development of catalysts that can harvest visible light and separate photo-generated charges efficiently [6,7]. Among available photocatalysts, g-C<sub>3</sub>N<sub>4</sub>, which is an analog of graphite, has received wide attention, because of its flexible layered structure, relatively narrow band gap of ~2.7 eV, reasonable production cost, and excellent durability [8]. However, the H<sub>2</sub>-evolution activity of pristine g-C<sub>3</sub>N<sub>4</sub> is limited owing to its low visible-light absorption, limited active sites, and high electron-hole recombination rate. Therefore, strategies such as dye-sensitization, construction of g-C<sub>3</sub>N<sub>4</sub>-based heterostructures with other semiconductors, and cocatalysts modification have been exploited to tackle these limitations [8–15]. In addition, given the identical sp<sup>2</sup>-bonded π structure exhibited between graphitic carbon and g-C<sub>3</sub>N<sub>4</sub>, coupling g-C<sub>3</sub>N<sub>4</sub> with graphitic carbon to construct composite has been developed to enhance the charge separation efficiency of g-C<sub>3</sub>N<sub>4</sub> [16–22]. Indeed,

an elaborate integration of graphitic carbon with g-C<sub>3</sub>N<sub>4</sub> possessing intimate coupling interfaces is necessary to achieve efficient charge separation [16].

When dye-sensitization techniques were employed to increase photocatalyst absorption in the visible-light region, cocatalysts used to accelerate electron transfer from excited dye molecules to active sites is essential [23–27]. Noble metal Pt is such an excellent cocatalyst [23–32], but rare and expensive, limiting its practical application. Then, some abundant earth catalysts, mostly nickel-based cocatalysts including Ni(OH)<sub>2</sub>, NiS<sub>x</sub>, Ni/graphene, and Ni/NiOx, were developed to replace Pt for accelerating electron transfer [33–40]. Our previous work demonstrated that nickel phosphide (Ni<sub>2</sub>P) was also an efficient cocatalyst to promote electron transport from excited dye molecules to active sites [11,12]. At present, transition metal phosphides are the most promising water splitting cocatalysts due to their light-harvesting and trapping electron abilities, as well as high catalytic reduction activity and durability [41,42]. Furthermore, it was proven that the encapsulation of metal phosphides in highly conductive carbon materials is an efficient strategy to construct a highly active and durable hybrid electrocatalyst for water splitting. This hybrid catalysts exhibit

\* Corresponding author.

E-mail address: [inorchemwl@126.com](mailto:inorchemwl@126.com) (L. Wang).

improved electrocatalytic performance in comparison with single metal phosphides owing to the synergistic effects among all components and improved electrical conductivity [43–46]. Thus, a controlled design of metal phosphides encapsulated in carbons may yield highly efficient photocatalysts able to promote the photo-generated electron transfer.

Designing a tight coupling interface between cocatalyst and semiconductor to maximize the charge separation and electron transfer rate is also useful for improving photocatalysts performances [47]. Metal-organic frameworks (MOFs), a class of porous materials with high surface area and tunable architecture, exhibit strong potential as templates and/or precursors for fabricating porous carbon materials via thermolysis [48–51]. Alloys and/or metal oxides covered with graphitic carbon also can be obtained by annealing of MOFs [52–62], which can be converted to metal phosphide/carbon composites via phosphidation [43,63,64]. In addition, MOFs can act as host matrices to anchor g-C<sub>3</sub>N<sub>4</sub> for the fabrication of MOF/g-C<sub>3</sub>N<sub>4</sub> composites with tight contact for efficient interfacial charge transfer [11,12,65–71]. Inspired by the above considerations, a Ni<sub>2</sub>P/Ni@carbon/g-C<sub>3</sub>N<sub>4</sub> composite was here developed: first, Ni-MOF/g-C<sub>3</sub>N<sub>4</sub> hybrids with tight contact were constructed via self-assembly technique; then, they were transformed to a hybrid nanostructure composed of Ni<sub>2</sub>P/Ni embedded in carbons via a pyrolysis-phosphidation method. The intimate contact among g-C<sub>3</sub>N<sub>4</sub>, in situ formed carbon materials, and electron-capture center of Ni<sub>2</sub>P/Ni nanoparticles (NPs) will improve the photo-generated charge transfer. In this work, we mostly focused on the design and synthesis of the Ni<sub>2</sub>P/Ni@carbon/g-C<sub>3</sub>N<sub>4</sub> composite, its inherent capability to efficiently separate electron-hole pairs and generate H<sub>2</sub> from photocatalytic water splitting under dye sensitization was also investigated.

We designed a novel composite composed of Ni<sub>2</sub>P/Ni NPs embedded in carbon/g-C<sub>3</sub>N<sub>4</sub> hybrids (Ni<sub>2</sub>P/Ni@C/g-C<sub>3</sub>N<sub>4</sub>) via pyrolysis and phosphidation of the Ni-MOF/g-C<sub>3</sub>N<sub>4</sub> precursor. H<sub>2</sub>-evolution measurement results suggested that this newly designed catalyst can indeed work as an efficient photocatalyst toward water splitting. The derived carbons can act as an electron transport bridge for efficient electron transfer from g-C<sub>3</sub>N<sub>4</sub> and excited EY to Ni<sub>2</sub>P/Ni NPs. Benefiting from the synergistic effect of Ni<sub>2</sub>P/Ni NPs and carbons, strong interfacial coupling effects among Ni<sub>2</sub>P/Ni, carbon, and g-C<sub>3</sub>N<sub>4</sub>, the resulting Ni<sub>2</sub>P/Ni@C/g-C<sub>3</sub>N<sub>4</sub> exhibits an excellent electron transfer ability for H<sub>2</sub> evolution: indeed, this composite has an H<sub>2</sub>-evolution rate equal to 18.04 mmol g<sup>-1</sup> h<sup>-1</sup> under 1.0 mmol L<sup>-1</sup> Eosin Y (EY)-sensitization, which is ~13 times higher than that of pristine g-C<sub>3</sub>N<sub>4</sub>. We also discussed the mechanism of the enhanced H<sub>2</sub> evolution performance over Ni<sub>2</sub>P/Ni@C/g-C<sub>3</sub>N<sub>4</sub> composite.

## 2. Experimental details

### 2.1. Preparation of Ni<sub>2</sub>P/Ni@C/g-C<sub>3</sub>N<sub>4</sub> composites

Ni-MOF was synthesized via a solvothermal method previously reported in the literature [57]. g-C<sub>3</sub>N<sub>4</sub> was obtained via thermal treatment of melamine precursor. Details for the synthesis of Ni-MOF and g-C<sub>3</sub>N<sub>4</sub> are provided in the Supplementary Materials.

Ni<sub>2</sub>P/Ni@C/g-C<sub>3</sub>N<sub>4</sub> composite was synthesized via a self-assembly-pyrolysis and phosphidation methods. First, 0.1 g of Ni-MOF was dispersed in 10 mL of 10 g L<sup>-1</sup> g-C<sub>3</sub>N<sub>4</sub> methanol suspension with constant stirring at 60 °C for 12 h. The Ni-MOF/g-C<sub>3</sub>N<sub>4</sub> precursor was obtained by evaporating methanol from this suspension. Then, the so-obtained Ni-MOF/g-C<sub>3</sub>N<sub>4</sub> powder was annealed under an N<sub>2</sub> atmosphere at 450, 500, 550, and 600 °C for 2 h with the heating speed of 2 °C min<sup>-1</sup> to obtain Ni@carbon/g-C<sub>3</sub>N<sub>4</sub> (Ni@C/g-C<sub>3</sub>N<sub>4</sub>) composite. Finally, the resulting Ni@C/g-C<sub>3</sub>N<sub>4</sub> and NaH<sub>2</sub>PO<sub>2</sub> with a mass ratio of 1:10 were placed at two separate positions (downstream and upstream, respectively) of the same quartz tube under constant N<sub>2</sub> flow. Then, the quartz tube was heated to 300 °C at a 2 °C min<sup>-1</sup> heating rate and held at this temperature for 120 min followed by naturally cooling to room temperature. The samples annealed at different temperatures (450, 500,

550, and 600 °C) were labeled as Ni<sub>2</sub>P/Ni@C/g-C<sub>3</sub>N<sub>4</sub>-450, Ni<sub>2</sub>P/Ni@C/g-C<sub>3</sub>N<sub>4</sub>-500, Ni<sub>2</sub>P/Ni@C/g-C<sub>3</sub>N<sub>4</sub>-550, Ni<sub>2</sub>P/Ni@C/g-C<sub>3</sub>N<sub>4</sub>-600, respectively. A sample without annealing was also obtained via a similar procedure and labeled as Ni<sub>2</sub>P@AC/g-C<sub>3</sub>N<sub>4</sub>.

### 2.2. Characterization

Powder X-ray diffraction (XRD) data were collected using a Rigaku D-MAX 2500/PC diffractometer equipped with a Cu K $\alpha$  radiation source. X-ray photoelectron spectra (XPS) were recorded using an X-ray photoelectron spectrometer (Thermo Scientific, K $\alpha$ ) equipped with a monochromatic Al K $\alpha$  X-ray source ( $h\nu = 1486.6$  eV). UV-vis diffuse reflectance spectra were recorded using a Lambda 750 UV/VIS/NIR spectrometer. The morphology of the so-obtained samples was investigated by using a TESCAN-VEGA3 scanning electron microscopy (SEM) instrument. High-angle annular dark field scanning TEM (HAADF-STEM) coupled with energy dispersive spectroscopy (EDS) elemental mapping were recorded by a Bruker super-X EDS. A Fluorescophotometer (F-4500 FL) was used to record photoluminescence (PL) spectra. Raman spectra were recorded at room temperature using a Renishaw InVia micro-Raman spectrometer with laser excitation at 532 nm.

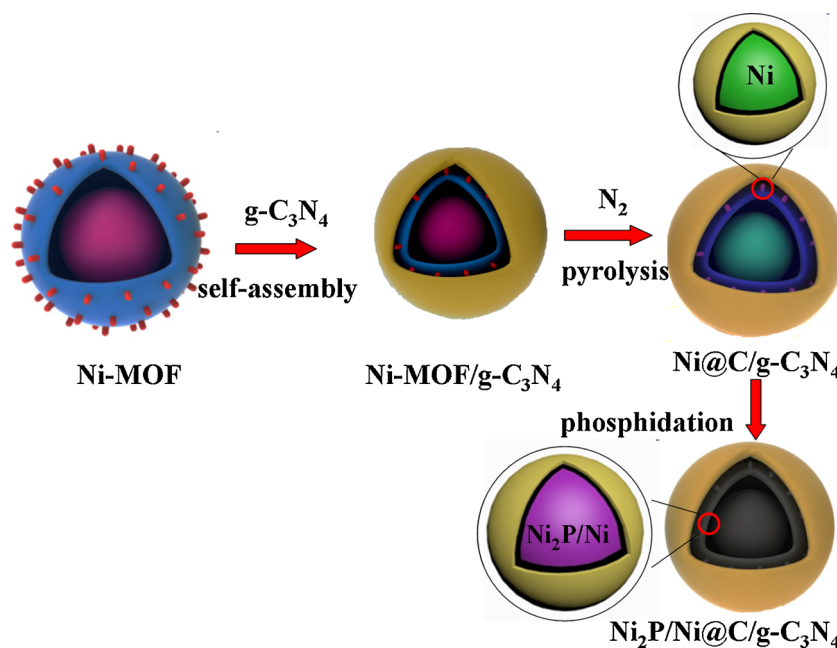
### 2.3. Photocatalytic activity for H<sub>2</sub> evolution

The photocatalytic reaction was carried out in a quartz flask equipped with a flat optical entry window. 10 mg of the photocatalyst was dispersed in 100 mL of an aqueous solution containing 10% of triethanolamine (TEOA) in volume as a sacrificial agent and 1 mmol L<sup>-1</sup> (except for studying the effect of EY concentration on H<sub>2</sub> evolution) of EY as the photosensitizer, and the system was deaerated by bubbling N<sub>2</sub> into the solution for 10 min before light irradiation. A 300-W Xe lamp with cut-off filter ( $\lambda \geq 420$  nm) was used as the visible-light source. The amount of H<sub>2</sub> evolved was determined at an interval of 1 h using an online gas chromatography system (GC-7920). The apparent quantum efficiency (AQE) was measured under the same photocatalytic reaction conditions on irradiating by using a 300-W Xe lamp with a 420 nm band pass filter. Photon flux of the incident light was determined using an optical power meter (Model: CEL-NP2000, Beijing China Education Au-Light Co., Ltd). In the AQE test, the reaction mixtures were irradiated for 60 min. AQE was calculated using the following equation:

$$\text{AQE} = \frac{2 \times \text{the number of evolved hydrogen molecules}}{\text{the number of incident photons}} \times 100\%$$

### 2.4. Photoelectrochemical measurements

Photocurrent measurements and Mott – Schottky (MS) plot analyses were performed using a CHI 660D electrochemical workstation (Chenhua Instrument, Shanghai, China) in a conventional three-electrode configuration using a Pt foil as the counter electrode and Ag/AgCl (saturated KCl) as the reference electrode. A 300-W Xe arc lamp (PLS-SXE300) was used as the light source. A 0.5 M Na<sub>2</sub>SO<sub>4</sub> aqueous solution was used as the electrolyte. The electrochemical impedance spectra (EIS) were measured via an IM6e electrochemical station (Zahner Elektrik, Germany) using the same three-electrode system. The working electrodes were prepared as follows: 5 mg of the photocatalyst was ground with 5  $\mu$ L of acetylacetone and 500  $\mu$ L of distilled water for 30 min, making a slurry. The slurry was then spread on a ITO glass substrate with an active area of about 1  $\times$  1 cm<sup>2</sup> using the doctor-blade method and an adhesive tape as the space. The electrode was dried in air and annealed at 200 °C for 30 min under N<sub>2</sub> atmosphere.



**Scheme 1.** Process of the formation of  $\text{Ni}_2\text{P}/\text{Ni}@\text{C}/\text{g-C}_3\text{N}_4$  composites.

### 3. Results and discussion

#### 3.1. Catalyst characterization

**Scheme 1** illustrates the synthetic process of the  $\text{Ni}_2\text{P}/\text{Ni}@\text{C}/\text{g-C}_3\text{N}_4$  composite. Ni-MOF was synthesized via a solvothermal method. The main diffraction peaks of the so-synthesized Ni-MOF are similar to those reported previously (Fig. S1a). SEM (Fig. S2a) and TEM (Fig. S2c) images reveal that Ni-MOF shows spherical hollow structures with a diameter of  $\sim 2 \mu\text{m}$ , which can be seen from the SEM image of the broken spheres, and some small crystalline needles anchored on its surfaces [57]. Then, the so-obtained Ni-MOF was used as a matrix to anchor  $\text{g-C}_3\text{N}_4$  sheets (Figs. 2f and 3 d) via a self-assembly process. Both diffraction peaks of  $\text{g-C}_3\text{N}_4$  and Ni-MOF were detected in the XRD pattern of Ni-MOF/ $\text{g-C}_3\text{N}_4$  (Fig. S1b). Partial needles on Ni-MOF/ $\text{g-C}_3\text{N}_4$  spheres were covered (Fig. S2b and d). The Ni@C/ $\text{g-C}_3\text{N}_4$  sample was obtained by pyrolysis of Ni-MOF/ $\text{g-C}_3\text{N}_4$  at various temperatures (450, 500, 550, and 600 °C) in flowing  $\text{N}_2$ . Carbonization temperatures were determined according to results reported previously to avoid the decomposition of  $\text{g-C}_3\text{N}_4$  [57,72]. As shown in the XRD pattern of Ni@C/ $\text{g-C}_3\text{N}_4$ -550 (Fig. S3b), three peaks located at 44.8°, 52.2°, and 76.8° can be observed, corresponding to the (111), (200), and (220) facets of Ni (PDF no. 4-0850). The weak peaks located at 26.3° and 42.0° can be assigned to the (002) and (201) facet of graphitic carbon. Peaks with 2θ values at 27.0° and 47.4° attributed to the (002) and (103) planes of  $\text{g-C}_3\text{N}_4$  are also present. SEM (Fig. S2e) and TEM (Fig. S2f) images indicate that the Ni@C/ $\text{g-C}_3\text{N}_4$ -550 has maintained their original spherical structure with a rough surface coated by the graphitic carbon. The formation of graphitic carbon was mainly attributed to the catalytic effect of Ni NPs during the pyrolysis process [57,73,74]. After the subsequent phosphidation in  $\text{N}_2$  with  $\text{NaH}_2\text{PO}_2$ , the Ni@C/ $\text{g-C}_3\text{N}_4$  composites are converted into the  $\text{Ni}_2\text{P}/\text{Ni}@\text{C}/\text{g-C}_3\text{N}_4$ . Energy dispersive X-ray (EDX) spectrum shows the presence of Ni, P, C, and N elements (Fig. S4). The corresponding XRD and morphology characterizations are shown in Figs. 1–3. The peaks at 40.7°, 44.6°, 47.4°, and 54.2° can be assigned to the (111), (201), (210), and (300) facets of  $\text{Ni}_2\text{P}$  (PDF no. 03-0953). The peaks of metallic Ni at 51.7° and 76.2° are also found in all the samples except the one that has not undergone the pyrolysis treatment (Fig. 1a), indicating that Ni NPs phosphidation is not complete. Furthermore, both two peaks of metallic Ni become more

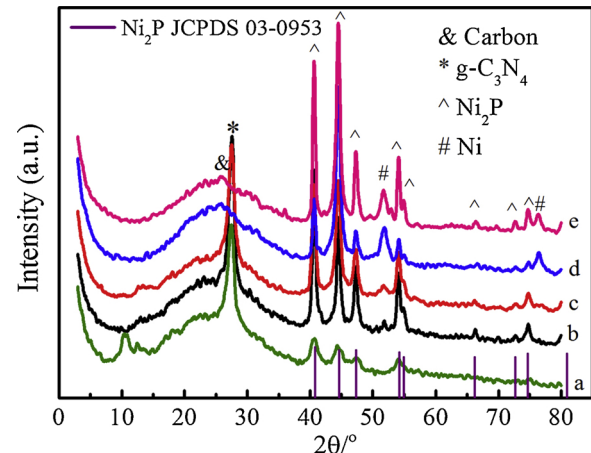


**Fig. 1.** XRD patterns of (a)  $\text{Ni}_2\text{P}@\text{AC}/\text{g-C}_3\text{N}_4$ , and  $\text{Ni}_2\text{P}/\text{Ni}@\text{C}/\text{g-C}_3\text{N}_4$  composites annealed at (b) 450, (c) 500, (d) 550, and (e) 600 °C.

intense with increasing pyrolysis temperature, indicating that more  $\text{Ni}^{2+}$  cations from the Ni-MOF precursor could be reduced to Ni NPs at a higher temperature during the second-pyrolysis process. The presence of low-intensity peaks of Ni in composite annealed at 450 °C ( $\text{Ni}@\text{C}/\text{g-C}_3\text{N}_4$ -450) further confirms this point (Fig. S3a). Additionally, the characteristic peak of  $\text{g-C}_3\text{N}_4$  at 27.7° becomes weaker after pyrolysis at 550 and 600 °C, but the widely broadened peak at 20–30° is more intense. It was reported that the strong decomposition of  $\text{g-C}_3\text{N}_4$  occurred as the temperature is higher than 600 °C [72]; however, the characteristic peaks of calcinated  $\text{g-C}_3\text{N}_4$  at 600 °C are still present but with increased peak intensity (Fig. S5), suggesting that its crystal structure is not destroyed. Therefore, the decreased peak intensity at 27.4° in samples annealed at 550 and 600 °C (Fig. 1d and e) indicates that the degree of crystallinity of  $\text{g-C}_3\text{N}_4$  has decreased and the distance between different layers of  $\text{g-C}_3\text{N}_4$  has increased [75]. After phosphidation, the spherical morphology of the Ni-MOF precursor also unchanged, but many carbon NPs are coated on the surface of  $\text{Ni}_2\text{P}/\text{Ni}@\text{C}/\text{g-C}_3\text{N}_4$  composites obtained at the 450 and 500 °C annealing temperatures (Fig. 2b and c), whereas nano-tubular carbon with a length of  $\sim 100 \text{ nm}$  are found on the surface of  $\text{Ni}_2\text{P}/\text{Ni}@\text{C}/\text{g-C}_3\text{N}_4$ -550

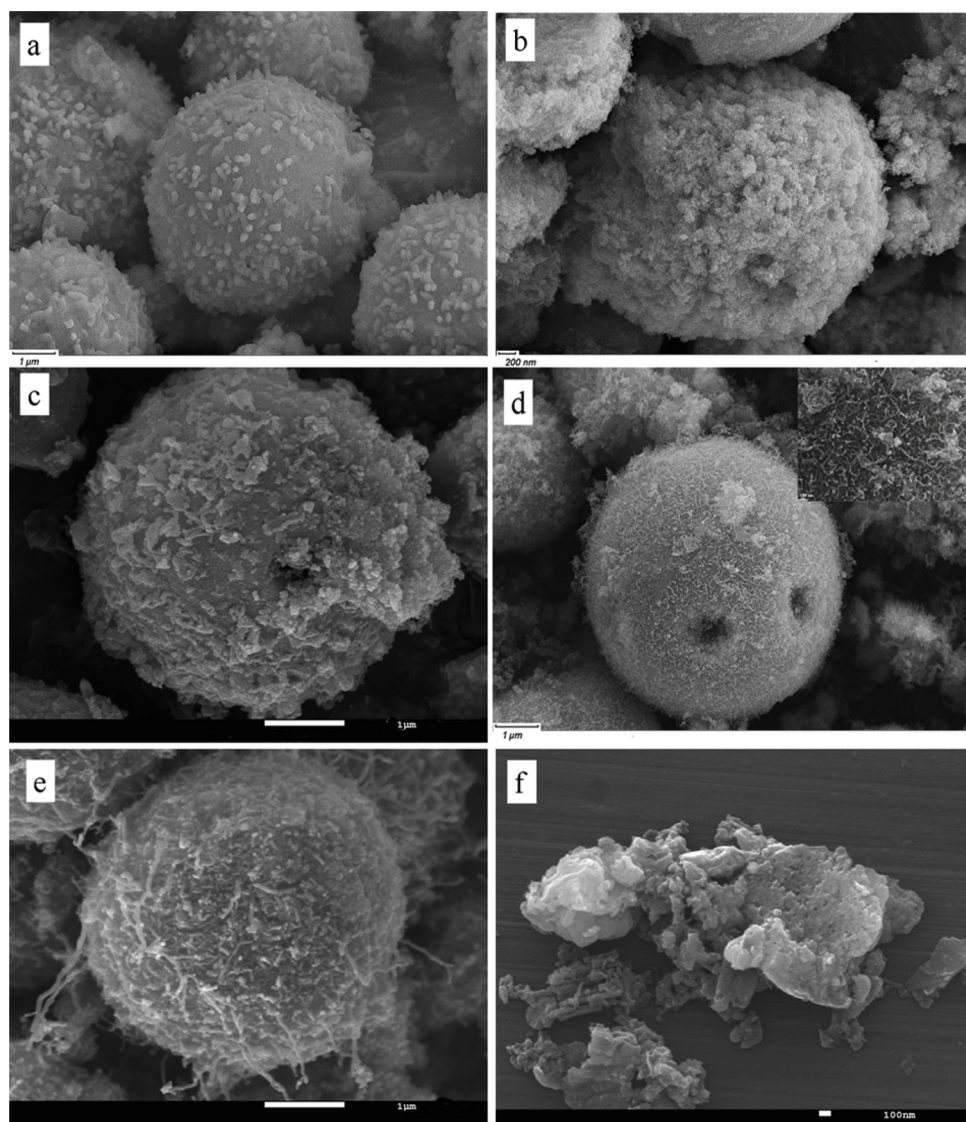


**Fig. 2.** SEM images of (a)  $\text{Ni}_2\text{P}@\text{AC}/\text{g-C}_3\text{N}_4$ , and  $\text{Ni}_2\text{P}/\text{Ni}@\text{C}/\text{g-C}_3\text{N}_4$  composites annealed at (b) 450, (c) 500, (d) 550, (e) 600  $^{\circ}\text{C}$ , and (f)  $\text{g-C}_3\text{N}_4$ .

(Fig. 2d). The  $\text{Ni}_2\text{P}/\text{Ni}@\text{C}/\text{g-C}_3\text{N}_4$ -600 surface exhibited similar nano-tubular carbon morphology but with length higher than 100 nm (Fig. 2e). For  $\text{Ni}_2\text{P}@\text{AC}/\text{g-C}_3\text{N}_4$  derived from Ni-MOF/ $\text{g-C}_3\text{N}_4$  without pyrolysis, crystalline needles anchored on amorphous carbon can be observed (Fig. 2a). These results further indicate that the transformation from amorphous carbon to graphitic carbon can be realized through catalytic graphitization by Ni NPs. HRTEM was employed to investigate the crystal properties of the  $\text{Ni}_2\text{P}/\text{Ni}@\text{CNT}/\text{g-C}_3\text{N}_4$ -550 composite (Fig. 3a). Crystal planes with  $d$ -spacing of 0.22, 0.20, and 0.40 nm, corresponding to the (111), (111), and (100) lattice planes of  $\text{Ni}_2\text{P}$ , Ni, and  $\text{g-C}_3\text{N}_4$ , respectively, are observed (Fig. 3c). The sphere-like nanostructures consist of  $\text{Ni}_2\text{P}$  or Ni cores, which are coated by nano-tubular carbon shell with an interlayer distance of 0.34 nm and  $\text{g-C}_3\text{N}_4$  (Fig. 3b). The diameter of  $\text{Ni}_2\text{P}$  or Ni NPs was  $\sim$  5–10 nm with uniform dispersion in the composite (Fig. 3b). In addition, intimate contact between carbon shell and  $\text{g-C}_3\text{N}_4$  was formed, which could be beneficial for a rapid electron transfer.

Fig. 4 shows the STEM-EDX elemental mapping images of  $\text{Ni}_2\text{P}/\text{Ni}@\text{C}/\text{g-C}_3\text{N}_4$ -550. A spherical morphology structure can be seen as the C, N, Ni, and P elements are uniformly distributed over the composite. Furthermore, the distribution density of C and N elements in the external part of the sphere is higher than inside, confirming that the  $\text{g-C}_3\text{N}_4$  has been anchored on Ni-MOF surface with tight contact.

The high-resolution XPS of the synthesized  $\text{Ni}_2\text{P}/\text{Ni}@\text{C}/\text{g-C}_3\text{N}_4$ -550 composite reveals that the binding energies (BEs) of Ni 2p located at 853.4 correspond to  $\text{Ni}^{\delta+}$  in  $\text{Ni}_2\text{P}$  or metallic Ni (Fig. 5a). Peaks at 855.3, 857.4, and 874.7 eV can be assigned to the oxidized Ni species ( $\text{Ni}^{2+}$ ) [76–79]. Peaks at 862.2 and 880.7 eV correspond to the satellite of the Ni 2p<sub>1/2</sub> and Ni 2p<sub>3/2</sub>. In addition, the peak at 870.7 eV is also ascribed to  $\text{Ni}^{\delta+}$  in  $\text{Ni}_2\text{P}$ . In the P 2p spectrum (Fig. 5d), peaks at 129.5, 130.0, and 133.0 eV correspond to the P 2p<sub>3/2</sub>, P 2p<sub>1/2</sub> in  $\text{Ni}_2\text{P}$  and oxidized P species, respectively. In the C 1s spectrum (Fig. 5b), the BE peaks at 284.6, 285.7, 286.1, and 288.0 eV are from C–C/C=C, C–N/C=N, C–O, and N–C=N bonds, respectively. Peaks at 398.3, 399.5, 401.0, and 404.2 eV in the N 1s spectrum (Fig. 5c) can be assigned to the BE of the pyridinic N/C=N=C, pyrrolic N/N–(C)<sub>3</sub>, graphitic N/C–N–H from  $\text{g-C}_3\text{N}_4$ , and  $\pi$ -excitation, respectively [64,80]. Thus, XPS confirms XRD results on the formation of  $\text{Ni}_2\text{P}/\text{Ni}@\text{C}/\text{g-C}_3\text{N}_4$  composite (Fig. S6).

The structure of the so-prepared  $\text{Ni}_2\text{P}/\text{Ni}@\text{C}/\text{g-C}_3\text{N}_4$  composites was further analyzed via Raman spectroscopy. All samples exhibit the characteristic carbon peaks located at 1343 and 1582  $\text{cm}^{-1}$ , corresponding to the D and G bands of graphitized carbon. The G band can be utilized to analyze the degree of graphitization, while the D band is associated with partial disorder or defects of the graphitic domains [81]. Therefore, the intensity ratio of D and G bands ( $I_{\text{D}}/I_{\text{G}}$ ) can be

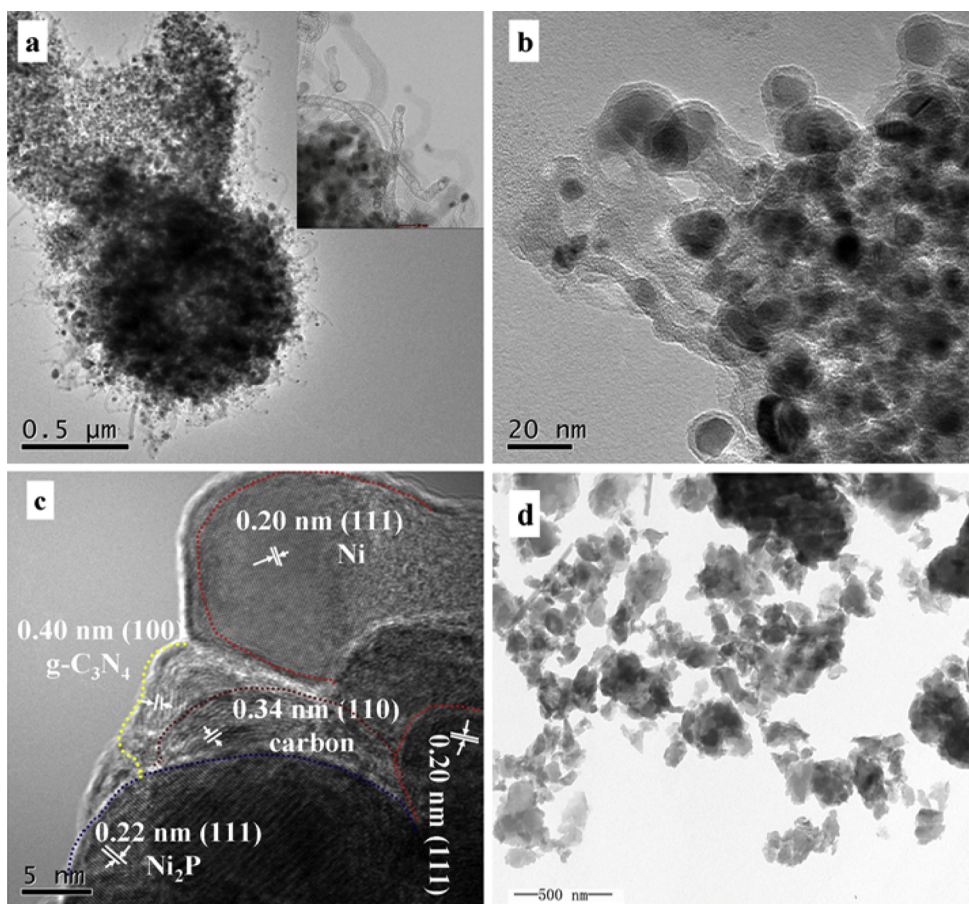


Fig. 3. TEM images of (a, b, and c)  $\text{Ni}_2\text{P}/\text{Ni}@\text{C}/\text{g-C}_3\text{N}_4$ -550 composite and (d)  $\text{g-C}_3\text{N}_4$ .

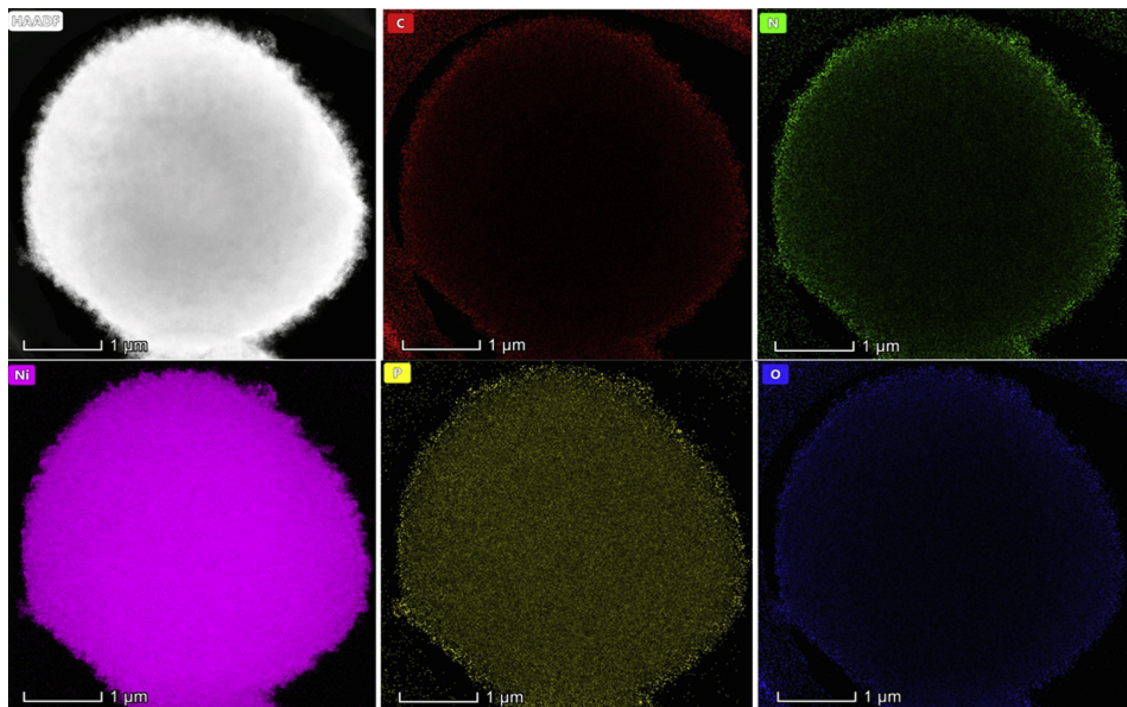


Fig. 4. STEM-EDX image of  $\text{Ni}_2\text{P}/\text{Ni}@\text{C}/\text{g-C}_3\text{N}_4$ -550 composite and the corresponding element mapping for C, N, Ni, P, and O.

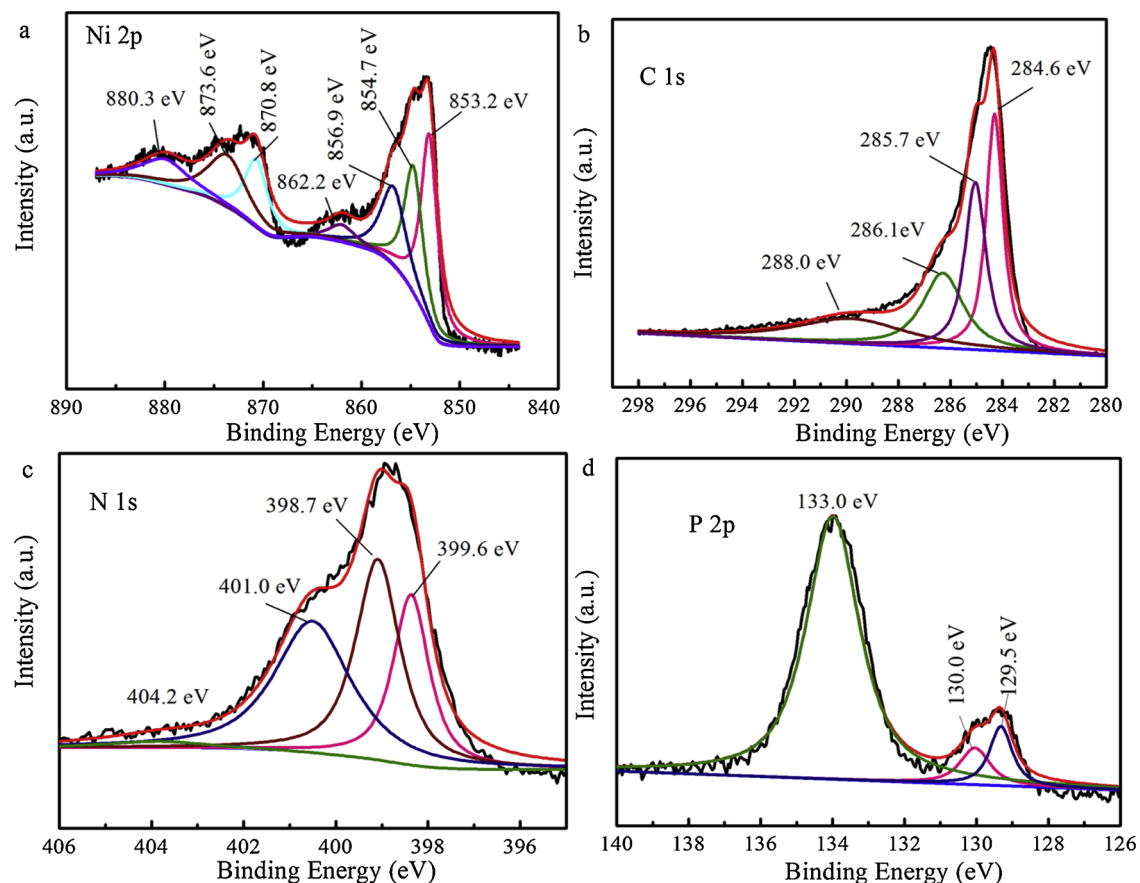


Fig. 5. High-resolution XPS of (a) Ni 2p, (b) C 1s, (c) N 1s, and (d) P 2p.

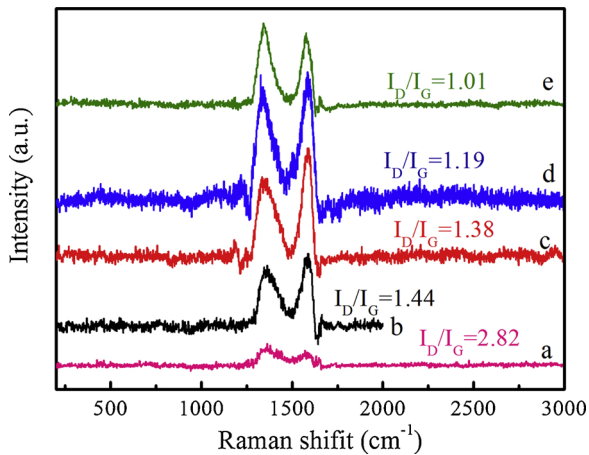


Fig. 6. Raman spectra of (a)  $\text{Ni}_2\text{P}@\text{AC}/\text{g-C}_3\text{N}_4$ , and  $\text{Ni}_2\text{P}/\text{Ni}@\text{C}/\text{g-C}_3\text{N}_4$  composites annealed at (b) 450, (c) 500, (d) 550, and (e) 600 °C.

determined to evaluate the amount of defects or the graphitization degree of carbon in composites. As shown in Fig. 6, the  $I_D/I_G$  values followed the order of  $\text{Ni}_2\text{P}/\text{Ni}@\text{C}/\text{g-C}_3\text{N}_4-600$  (1.01) <  $\text{Ni}_2\text{P}/\text{Ni}@\text{C}/\text{g-C}_3\text{N}_4-550$  (1.19) <  $\text{Ni}_2\text{P}/\text{Ni}@\text{C}/\text{g-C}_3\text{N}_4-500$  (1.38) <  $\text{Ni}_2\text{P}/\text{Ni}@\text{C}/\text{g-C}_3\text{N}_4-450$  (1.44) <  $\text{Ni}_2\text{P}@\text{C}/\text{g-C}_3\text{N}_4$  (2.82). The low  $I_D/I_G$  values for samples  $\text{Ni}_2\text{P}/\text{Ni}@\text{C}/\text{g-C}_3\text{N}_4-550$  and  $\text{Ni}_2\text{P}/\text{Ni}@\text{C}/\text{g-C}_3\text{N}_4-600$  indicate that an increase in the pyrolysis temperature can lead to higher graphitization degree of the carbon phase owing to the increased Ni NPs contents, which has high conductivity and beneficial for electron transfer.

The optical response properties of the so-prepared composites are displayed in Fig. 7. EY shows an evident absorption in the range of

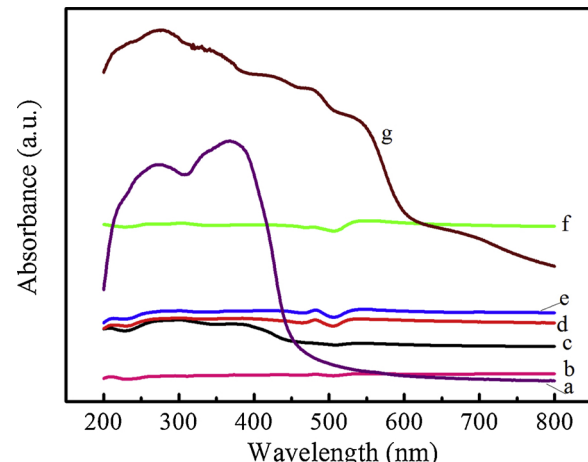
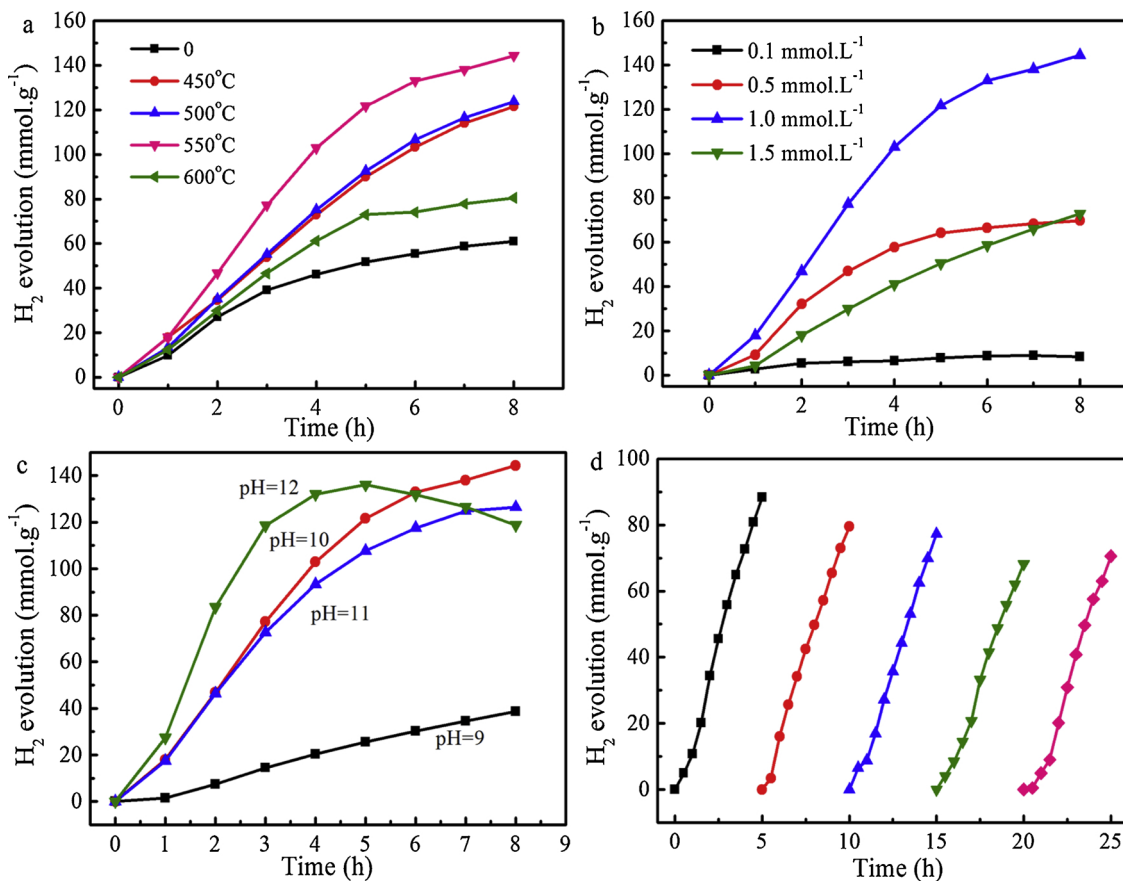
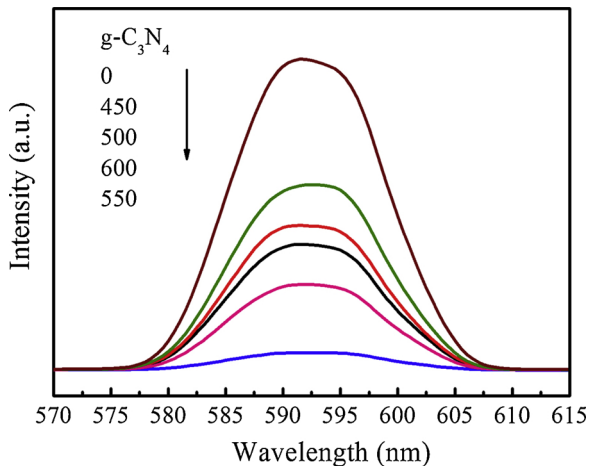


Fig. 7. UV-vis diffuse reflectance spectra of the (a)  $\text{g-C}_3\text{N}_4$ , (b)  $\text{Ni}_2\text{P}@\text{AC}/\text{g-C}_3\text{N}_4$ ,  $\text{Ni}_2\text{P}/\text{Ni}@\text{C}/\text{g-C}_3\text{N}_4$  composites annealed at (c) 450, (d) 500, (e) 550, (f) 600 °C, and (g) EY.

200–800 nm (Fig. 7), whereas the  $\text{Ni}_2\text{P}@\text{AC}/\text{g-C}_3\text{N}_4$  catalyst obtained via a direct phosphidation of Ni-MOF/ $\text{g-C}_3\text{N}_4$  exhibits a low light absorption in the same range. After the pyrolysis of Ni-MOF/ $\text{g-C}_3\text{N}_4$  at 450–600 °C and then phosphidation, the obtained  $\text{Ni}_2\text{P}/\text{Ni}@\text{C}/\text{g-C}_3\text{N}_4$  composites show enhanced light absorption, which is because of the decreased light reflection and accelerated electron transport caused by the formed carbon materials [20], as well as the light-harvesting performance of  $\text{Ni}_2\text{P}/\text{Ni}$  NPs. Moreover, the visible-light absorption intensity of these composites increases with the pyrolysis temperature due to the increased conductivity of carbons and Ni contents.



**Fig. 8.** (a) H<sub>2</sub> amounts produced over Ni<sub>2</sub>P@AC/g-C<sub>3</sub>N<sub>4</sub> and Ni<sub>2</sub>P/Ni@C/g-C<sub>3</sub>N<sub>4</sub> composites annealed at 450, 500, 550, and 600 °C; effects of (b) EY concentration, (c) solution pH on H<sub>2</sub> amounts over Ni<sub>2</sub>P/Ni@C/g-C<sub>3</sub>N<sub>4</sub>-550 composite, and (d) five consecutive experiments measuring the amounts of H<sub>2</sub> evolved over the same Ni<sub>2</sub>P/Ni@C/g-C<sub>3</sub>N<sub>4</sub>-550 composite cleaned between the experiments.



**Fig. 9.** PL spectra of the EY-sensitized g-C<sub>3</sub>N<sub>4</sub>, Ni<sub>2</sub>P@AC/g-C<sub>3</sub>N<sub>4</sub> and Ni<sub>2</sub>P/Ni@C/g-C<sub>3</sub>N<sub>4</sub> composites annealed at 450, 500, 550, and 600 °C.

### 3.2. Catalytic performance

Photocatalytic H<sub>2</sub> evolution of the so-prepared composites was determined in the presence of 10% triethanolamine (TEOA), as a sacrificial agent for capturing holes, and 1.0 mmol L<sup>-1</sup> of EY, as a photosensitizer (Fig. 8). Control experiments showed a small amount of H<sub>2</sub> (1.33 mmol g<sup>-1</sup> h<sup>-1</sup>) when pristine g-C<sub>3</sub>N<sub>4</sub> was used. The rate of H<sub>2</sub> production over Ni<sub>2</sub>P@AC/g-C<sub>3</sub>N<sub>4</sub> has reached 7.64 mmol g<sup>-1</sup> h<sup>-1</sup> (Fig. 8a and Table S1), 5.7 times higher than that of the pristine g-C<sub>3</sub>N<sub>4</sub>.

When Ni-MOF/g-C<sub>3</sub>N<sub>4</sub> has been annealed at 450 °C and then phosphidated to produce Ni<sub>2</sub>P/Ni@C/g-C<sub>3</sub>N<sub>4</sub>-450 composite, the H<sub>2</sub>-evolution rate is 15.19 mmol g<sup>-1</sup> h<sup>-1</sup>. This indicates that Ni species and graphitic carbon are the indispensable active sites to promote the H<sub>2</sub> evolution. By increasing the pyrolysis temperature to 500 °C, the H<sub>2</sub>-evolution rate slightly increases to 15.47 mmol g<sup>-1</sup> h<sup>-1</sup>. The optimal H<sub>2</sub>-evolution rate of 18.04 mmol g<sup>-1</sup> h<sup>-1</sup> is achieved when Ni-MOF/g-C<sub>3</sub>N<sub>4</sub> has been annealed at 550 °C (Ni<sub>2</sub>P/Ni@C/g-C<sub>3</sub>N<sub>4</sub>-550), which is the double of that over the pyrolysis-free Ni<sub>2</sub>P@AC/g-C<sub>3</sub>N<sub>4</sub>. It indicates that the synergistic effects of increased Ni NPs content (Fig. 1) and improved conductivity (Raman plots), which is resulting from the higher graphitization degree of carbons, can more efficiently separate photo-generated electron-hole pairs (Figs. 9 and 10) and enhance the H<sub>2</sub>-evolution rate. The amount of H<sub>2</sub> evolved over Ni<sub>2</sub>P/Ni@C/g-C<sub>3</sub>N<sub>4</sub>-550 during the 8 h experiment is 144.308 mmol g<sup>-1</sup>, while the AQE of 58.1% is achieved at 420 nm A further increase in the pyrolysis temperature to 600 °C results in the decrease in the H<sub>2</sub>-evolution rate to 10.04 mmol g<sup>-1</sup> h<sup>-1</sup>. The Ni<sub>2</sub>P/Ni@C/g-C<sub>3</sub>N<sub>4</sub>-600 with the highest graphitization degree presents a lower activity than Ni<sub>2</sub>P/Ni@C/g-C<sub>3</sub>N<sub>4</sub>-550 was due to the limited electron transfer (Figs. 9 and 10) caused by agglomeration of Ni NPs occurred at high annealing temperature [62].

In addition, the H<sub>2</sub>-evolution activity over Ni<sub>2</sub>P/Ni@C/g-C<sub>3</sub>N<sub>4</sub>-550 is influenced by EY concentration and solution pH. As shown in Fig. 8b, a very small amount of H<sub>2</sub> (0.21 mmol g<sup>-1</sup> h<sup>-1</sup>) can be detected without EY-sensitization. Indeed, the H<sub>2</sub>-evolution activity of Ni<sub>2</sub>P/Ni@C/g-C<sub>3</sub>N<sub>4</sub>-550 has been enhanced to 1.27 mmol g<sup>-1</sup> h<sup>-1</sup> when 0.1 mmol L<sup>-1</sup> EY has been added. A further increase in EY concentration to 0.5 and 1.0 mmol L<sup>-1</sup> results in a largely enhanced H<sub>2</sub>-evolution rate (7.97 and 18.04 mmol g<sup>-1</sup> h<sup>-1</sup>, respectively), but which then

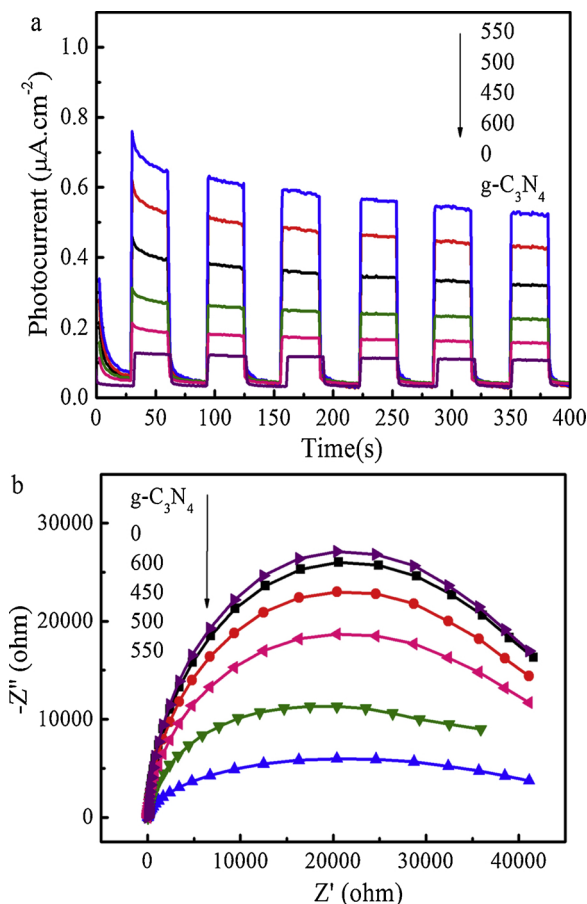


**Fig. 10.** (a) Transient photocurrent responses and (b) EIS curves of the electrodes composed of g-C<sub>3</sub>N<sub>4</sub>, Ni<sub>2</sub>P@AC/g-C<sub>3</sub>N<sub>4</sub>, and Ni<sub>2</sub>P/Ni@C/g-C<sub>3</sub>N<sub>4</sub> composites annealed at 450, 500, 550, and 600 °C.

decreases to 9.70 mmol g<sup>-1</sup> h<sup>-1</sup> under 1.5 mmol L<sup>-1</sup> EY-sensitization due to the self-quenching and shielding effect of the incident photons by EY [82]. Previous studies confirmed that the pH in the dye-sensitized photocatalysis systems could change the existing states of the dye and TEOA [83], which then influences the H<sub>2</sub>-evolution rate. As shown in Fig. 8c, the H<sub>2</sub>-evolution rate (18.03 mmol g<sup>-1</sup> h<sup>-1</sup>) over Ni<sub>2</sub>P/Ni@C/g-C<sub>3</sub>N<sub>4</sub>-550 is highest at natural pH of 10. A pH higher than 10 leads to the decrease in H<sub>2</sub>-evolution rate likely due to the decreased H<sup>+</sup> concentration and thermodynamic driving force for H<sub>2</sub> evolution, as well as increased electrostatic repulsion forces between deprotonated EY and negatively charged g-C<sub>3</sub>N<sub>4</sub>. Lowering the pH to 9 leads to the decrease in the H<sub>2</sub>-evolution rate as a consequence of the protonation of TEOA [83], which becomes a less effective electron donor. The H<sub>2</sub>-evolution rate rapidly increases at pH of 12 during the 4 h experiment is due to the fast oxidation of TEOA; afterward, it decreases due to the extremely fast oxidation of TEOA, which is adverse for stable water splitting.

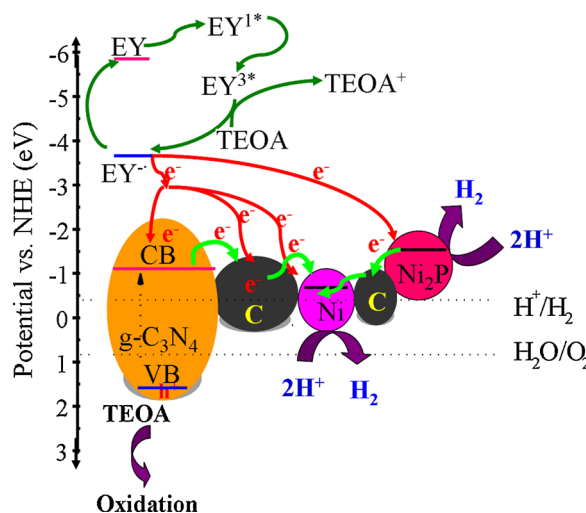
The stability of Ni<sub>2</sub>P/Ni@C/g-C<sub>3</sub>N<sub>4</sub>-550 was also evaluated by performing recycling experiments. At the end of each run residual H<sub>2</sub> produced during prior experiments was removed from the reaction cell. 0.5 mL TEOA and 0.5 mL 0.1 mmol L<sup>-1</sup> EY were added prior to the third and fourth run, and 0.5 mL TEOA was added in the fifth run. As shown in Fig. 8d, no significant decrease in H<sub>2</sub> evolution amount can be observed in five consecutively repeated experiments performed within the 25 h period. The XRD patterns of fresh and used Ni<sub>2</sub>P/Ni@C/g-C<sub>3</sub>N<sub>4</sub>-550 are identical (Fig. S7), indicating that the obtained Ni<sub>2</sub>P/Ni@C/g-C<sub>3</sub>N<sub>4</sub> composites possess good stability in photocatalytic H<sub>2</sub> evolution from water splitting.

### 3.3. Mechanism

The light-induced charge transfer of the so-prepared composites was discussed by analyzing their PL spectra, transient photocurrent, and EIS. As shown in Fig. 9, EY-sensitized g-C<sub>3</sub>N<sub>4</sub> excited at 593 nm shows a strong PL emission peak centered at ~ 580 nm. The coupling of g-C<sub>3</sub>N<sub>4</sub> with Ni-MOF to obtain Ni<sub>2</sub>P@AC/g-C<sub>3</sub>N<sub>4</sub> by direct phosphidation has weakened its PL peak intensity, indicating the electron transfer from photo-excited EY and g-C<sub>3</sub>N<sub>4</sub> to amorphous carbon-coated Ni<sub>2</sub>P. The PL peak intensity further decreases after annealing and phosphidation of the Ni-MOF/g-C<sub>3</sub>N<sub>4</sub> precursor, and the so-obtained Ni<sub>2</sub>P/Ni@C/g-C<sub>3</sub>N<sub>4</sub>-550 shows the lowest PL peak intensity, revealing that Ni-MOF-derived carbons with higher graphitization degree (Raman results) together with Ni<sub>2</sub>P/Ni NPs could favor the electron transfer. It should be noticed that, although increasing the pyrolysis temperature will lead to a higher graphitization degree of the carbons, a high pyrolysis temperature also results the agglomeration of Ni NPs [62], which would then block the electron transfer. This is the reason that the PL peak intensity increases again in the EY-sensitized Ni<sub>2</sub>P/Ni@C/g-C<sub>3</sub>N<sub>4</sub>-600 system. For the transient photocurrent of so-prepared composites, EY-sensitized g-C<sub>3</sub>N<sub>4</sub> exhibits the lowest photocurrent of 0.12 μA cm<sup>-2</sup>. The photocurrent has increased to 0.18 μA cm<sup>-2</sup> after phosphidation of Ni-MOF/g-C<sub>3</sub>N<sub>4</sub> to obtain the Ni<sub>2</sub>P@AC/g-C<sub>3</sub>N<sub>4</sub> composite. The highest photocurrent of 0.55 μA cm<sup>-2</sup> can be obtained in the EY-sensitized Ni<sub>2</sub>P/Ni@C/g-C<sub>3</sub>N<sub>4</sub>-550 composite, indicating the most efficient transfer of charge carriers corresponds to the best photocatalytic activity in the water-splitting reaction (Fig. 10a). Furthermore, EIS was also performed to evaluate the charge transfer resistance. The Nyquist plots given in Fig. 10b reveal that Ni<sub>2</sub>P/Ni@C/g-C<sub>3</sub>N<sub>4</sub>-550 has the smallest charge transfer resistance in comparison with g-C<sub>3</sub>N<sub>4</sub> and other composites, in agreement with the PL and transient photocurrent tests. All of these results highlight the highly graphitized carbons combined with the highly dispersed Ni<sub>2</sub>P/Ni NPs lead to efficient separation of photo-generated electron-hole pairs from the EY-sensitized g-C<sub>3</sub>N<sub>4</sub>.

To further understand how Ni<sub>2</sub>P/Ni NPs and carbon improve charge-separation efficiency and photocatalytic H<sub>2</sub> evolution in the Ni<sub>2</sub>P/Ni@C/g-C<sub>3</sub>N<sub>4</sub> composites, the band alignments of g-C<sub>3</sub>N<sub>4</sub>, Ni<sub>2</sub>P, Ni<sub>2</sub>P@AC/g-C<sub>3</sub>N<sub>4</sub>, and Ni<sub>2</sub>P/Ni@C/g-C<sub>3</sub>N<sub>4</sub>-550 were determined. According to the Tauc plots of (chv)<sup>2</sup> vs. photon energy (hv) (Fig. S8) and UV-vis absorption spectra (Fig. 5), the band gaps (E<sub>g</sub>) of g-C<sub>3</sub>N<sub>4</sub>, Ni<sub>2</sub>P@AC/g-C<sub>3</sub>N<sub>4</sub>, and Ni<sub>2</sub>P/Ni@C/g-C<sub>3</sub>N<sub>4</sub>-550 are calculated to be 2.68, 2.16, and 2.26 eV. Fig. S9 shows the MS plots of g-C<sub>3</sub>N<sub>4</sub>, Ni<sub>2</sub>P, Ni<sub>2</sub>P@AC/g-C<sub>3</sub>N<sub>4</sub>, and Ni<sub>2</sub>P/Ni@C/g-C<sub>3</sub>N<sub>4</sub>-550, the positive tangent slopes reveal that g-C<sub>3</sub>N<sub>4</sub> exhibited the typical characteristics of n-type semiconductors. The flat band potentials are -1.18, -1.26, -0.53, and -0.47 eV versus Ag/AgCl for g-C<sub>3</sub>N<sub>4</sub>, Ni<sub>2</sub>P, Ni<sub>2</sub>P@AC/g-C<sub>3</sub>N<sub>4</sub>, and Ni<sub>2</sub>P/Ni@C/g-C<sub>3</sub>N<sub>4</sub>-550, respectively. Generally, the conduction band (CB) potential for n-type semiconductor is more negative ( $\sim$  -0.2 eV) than its flat band potential [77,84,85] with E<sub>NHE</sub> = E<sub>Ag/AgCl</sub> + 0.197 [86]. Thus, the CB potentials for g-C<sub>3</sub>N<sub>4</sub>, Ni<sub>2</sub>P, Ni<sub>2</sub>P@AC/g-C<sub>3</sub>N<sub>4</sub>, and Ni<sub>2</sub>P/Ni@C/g-C<sub>3</sub>N<sub>4</sub>-550 are -1.18, -1.26, -0.53, and -0.47 eV vs. normal hydrogen electrode (NHE). Then, the valence band (VB) potentials of g-C<sub>3</sub>N<sub>4</sub>, Ni<sub>2</sub>P@AC/g-C<sub>3</sub>N<sub>4</sub>, and Ni<sub>2</sub>P/Ni@C/g-C<sub>3</sub>N<sub>4</sub>-550 are 1.50, 1.63, 1.79 V vs. NHE. The low VB value of Ni<sub>2</sub>P/Ni@C/g-C<sub>3</sub>N<sub>4</sub>-550 compared to Ni<sub>2</sub>P@AC/g-C<sub>3</sub>N<sub>4</sub> is due to the increased conductivity of carbon [20]. In general, a lower VB potential of semiconductor means stronger oxidation ability for TEOA, which can further facilitate the separation of electron-hole pairs, then enhance the H<sub>2</sub>-evolution activity.

Based on the above mentioned experimental results, a possible underlying mechanism of photocatalytic H<sub>2</sub> evolution by the Ni<sub>2</sub>P/Ni@C/g-C<sub>3</sub>N<sub>4</sub> composite, using EY as a photosensitizer, is presented in Scheme 2. Under visible-light illumination, EY absorbs light photons to form a singlet excited state EY<sup>1\*</sup>. Then, it forms EY<sup>3\*</sup> by intersystem crossing (ISC). EY<sup>3\*</sup> is quenched by TEOA to produce TEOA<sup>+</sup> and EY<sup>-</sup> [87,88]. Simultaneously, electrons in the VB of g-C<sub>3</sub>N<sub>4</sub> can be excited to the CB.



**Scheme 2.** Photocatalytic mechanism for  $H_2$  evolution over the EY-sensitized  $Ni_2P/Ni@C/g-C_3N_4$  composite with TEOA as a sacrificial agent under visible-light irradiation.

Previous works determined that the HOMO and LUMO levels of EY and excited EY are  $-5.60$  and  $-3.45$  eV [82]. The facts that the LUMO level of excited EY is more negative than the CB levels of  $g-C_3N_4$  and  $Ni_2P$ , as well as the over-potential of the metallic Ni ( $-1.0$  V vs. Ag/AgCl [89]) are favorable for the electrons transfer from  $EY^-$  to the CB of  $g-C_3N_4$ ,  $Ni_2P$  and Ni NPs. Moreover, metallic Ni can capture the electrons accumulated in CB of  $g-C_3N_4$  and  $Ni_2P$  because of the lower CB potentials of  $g-C_3N_4$  and  $Ni_2P$  compared to Ni NPs. The introduced carbons between  $g-C_3N_4$  and  $Ni_2P/Ni$  NPs can act as electron-transport bridges to accelerate the electron transfer due to their excellent electronic conductivity and tight contact, thus resulting in enhanced electron-hole separation efficiency and photocatalytic  $H_2$ -evolution performance. The charge transfer pathway between  $g-C_3N_4$  and  $Ni_2P/Ni@C$  can be demonstrated by decreasing the PL intensity and increasing the transient photocurrent. CB-electrons of  $g-C_3N_4$ , as well as electrons accumulated on  $Ni_2P$  and Ni can reduce  $H^+$  to generate  $H_2$ . The holes in  $g-C_3N_4$  can be consumed by TEOA because its redox potential ( $-0.84$  eV) is lower than the VB potential of  $g-C_3N_4$  ( $1.50$  eV) and its increased oxidation ability.

Control experiments showed that the  $H_2$ -evolution rates are  $2.89$ ,  $6.97$ , and  $7.99$  mmol  $g^{-1} h^{-1}$  over  $Ni_2P$ ,  $Ni_2P@C$ , and  $Ni_2P/Ni@C-550$  (Fig. S10), and a relatively slow  $H_2$ -evolution rate of  $5.40$  mmol  $g^{-1} h^{-1}$  over  $Ni@C/g-C_3N_4-550$  without phosphidation when compared with the  $Ni_2P/Ni@C/g-C_3N_4-550$  system ( $18.04$  mmol  $g^{-1} h^{-1}$ ), indicating that constructing  $Ni_2P/Ni$  heterogeneous cocatalyst combined with carbon can facilitate electrons transfer, increasing  $H_2$ -evolution activity.  $Ni_2P/Ni$  encapsulated in carbons may play the following roles in enhancing the  $H_2$ -evolution activity of  $g-C_3N_4$ : i) enhance the light absorption intensity of  $g-C_3N_4$ ; ii)  $Ni_2P$  together with Ni can act as an electron collector to capture electrons from excited EY and CB of  $g-C_3N_4$ , as well as serve as reaction active sites for  $H_2$  generation; iii) the hybridized carbons can act as an electron transport bridge to accelerate the charge transfer and increase the  $g-C_3N_4$  oxidation ability for TEOA.

#### 4. Conclusions

$Ni_2P/Ni$  NPs encapsulated in carbon/ $g-C_3N_4$  hybrids derived from pyrolysis and phosphidation of Ni-MOF/ $g-C_3N_4$  was fabricated for photocatalytic  $H_2$ -evolution from water splitting. Compared to  $g-C_3N_4$ ,  $Ni_2P@AC/g-C_3N_4$ ,  $Ni@C/g-C_3N_4-550$ ,  $Ni_2P/Ni/C/g-C_3N_4-550$  exhibited the highest photocatalytic activity with a  $H_2$ -evolution rate equal to  $18.04$  mmol  $g^{-1} h^{-1}$  under EY-sensitization. Its apparent quantum efficiency was  $58.1\%$  at  $420$  nm. This enhanced photocatalytic activity

can be attributed to the efficient separation of photo-induced electrons from excited EY and  $g-C_3N_4$  to Ni and  $Ni_2P$  NPs through carbon bridge owing to their tight contact, higher conductivity of in situ formed carbons, staggered band energy between  $g-C_3N_4$ , Ni and  $Ni_2P$ , and promoted  $H^+$  reduction reaction on Ni and  $Ni_2P$  NPs. This work provides new insights into the utilization of MOF-derived hybrid cocatalysts as substitutes to noble metals for effective photocatalytic  $H_2$  production.

#### Acknowledgements

The authors would like to thank the National Natural Science Foundation of China (No. 51404143, 51372125, 21571112), the Taishan Scholars Program.

#### Appendix A. Supplementary data

Supplementary material related to this article can be found, in the online version, at doi:<https://doi.org/10.1016/j.apcatb.2019.01.045>.

#### References

- [1] X.B. Chen, S.H. Shen, L.J. Guo, S.S. Mao, Chem. Rev. 110 (2010) 6503–6570.
- [2] M.D. Karkas, O. Verho, E.V. Johnston, B. Åkermark, Chem. Rev. 114 (2014) 11863–12001.
- [3] H. Wang, L. Zhang, Z. Chen, J. Hu, S. Li, Z. Wang, J. Liu, X. Wang, Chem. Soc. Rev. 43 (2014) 5234–5244.
- [4] B. Luo, G. Liu, L.Z. Wang, Nanoscale 8 (2016) 6904–6920.
- [5] S.Y. Tee, K.Y. Win, W.S. Teo, L.D. Koh, S.H. Liu, C.P. Teng, M.Y. Han, Adv. Sci. 4 (2017) 1600337–1600360.
- [6] J. Ran, J. Zhang, J. Yu, M. Jaroniec, S.Z. Qiao, Chem. Soc. Rev. 43 (2014) 7787–7812.
- [7] Y. Shi, B. Zhang, Chem. Soc. Rev. 45 (2016) 1529–1541.
- [8] A. Naseri, M. Samadi, A. Pourjavadi, A.Z. Moshfegh, S. Ramakrishna, J. Mater. Chem. A 5 (2017) 23406–23433.
- [9] X.H. Zhang, T.Y. Peng, L.J. Yu, R.J. Li, Q.Q. Li, Z. Li, ACS Catal. 5 (2015) 504–510.
- [10] S.X. Min, G.X. Lu, J. Phys. Chem. C 116 (2012) 19644–19652.
- [11] J.X. Xu, J.Y. Gao, Y.H. Qi, C. Wang, L. Wang, ChemCatChem 10 (2018) 3327–3335.
- [12] J.X. Xu, Y.H. Qi, C. Wang, L. Wang, Appl. Catal. B: Environ. 241 (2019) 178–186.
- [13] H.Y. Zhang, S. Li, R. Lu, A.C. Yu, ACS Appl. Mater. Interface 7 (2015) 21868–21874.
- [14] Z.J. Wang, Z.L. Jin, H. Yuan, G.R. Wang, B.Z. Ma, J. Colloid Interface Sci. 532 (2018) 287–299.
- [15] Y.P. Zhang, Z.L. Jin, Y.F. Su, G.R. Wang, Mol. Catal. 462 (2019) 46–55.
- [16] W.J. Ong, L.L. Tan, S.P. Chai, S.T. Yong, A.R. Mohamed, Nano Energy 13 (2015) 757–770.
- [17] R.W. Wang, T.T. Yan, L.P. Han, G.R. Chen, H.R. Li, J.P. Zhang, L.Y. Shi, D.S. Zhang, J. Mater. Chem. A 6 (2018) 5752–5761.
- [18] W.J. Ong, L.L. Tan, S.P. Chai, S.T. Yong, Chem. Commun. 51 (2015) 858–861.
- [19] Y.J. Yuan, Y. Yang, Z.J. Li, D.Q. Chen, S.T. Wu, G.L. Fang, W.F. Bai, M.Y. Ding, L.X. Yang, D.P. Cao, Z.T. Yu, Z.G. Zou, ACS Appl. Energy Mater. 1 (2018) 1400–1407.
- [20] J.Q. Wen, J. Xie, Z.H. Yang, R.C. Shen, H.Y. Li, X.Y. Luo, X.B. Chen, X. Li, ACS Sustain. Chem. Eng. 5 (2017) 2224–2236.
- [21] J. Liang, Y. Zheng, J. Chen, J. Liu, D. Hulicova-Jurcakova, M. Jaroniec, S.Z. Qiao, Angew. Chem. Int. Ed. 51 (2012) 3892–3896.
- [22] Q. Han, N. Chen, J. Zhang, L.T. Qu, Mater. Horiz. 4 (2017) 832–850.
- [23] X.H. Zhang, T.Y. Peng, S.S. Song, J. Mater. Chem. A 4 (2016) 2365–2402.
- [24] P. Chowdhury, G. Malekshoar, A.K. Ray, Inorganics 5 (2017) 34–68.
- [25] M. Watanabe, Sci. Technol. Adv. Mater. 18 (2017) 1705–1723.
- [26] J. Willkomm, K.L. Orchard, A. Reynal, E. Pastor, J.R. Durrant, E. Reisner, Chem. Soc. Rev. 45 (2016) 9–23.
- [27] K. Fan, Z.L. Jin, G.R. Wang, H. Yang, D.D. Liu, H.Y. Hu, G.X. Lu, Y.P. Bi, Catal. Sci. Technol. 8 (2018) 2352–2363.
- [28] S.X. Min, G.X. Lu, Int. J. Hydrogen Energy 37 (2012) 10564–10574.
- [29] T. Sreethawongsa, S. Yoshikawab, Chem. Eng. J. 197 (2012) 272–282.
- [30] Y. Xue, Y.G. Lei, X.Y. Liu, Y.N. Li, W.N. Deng, F. Wang, S.X. Min, New J. Chem. 42 (2018) 14083–14086.
- [31] R. Abe, K. Sayama, H. Arakawa, Chem. Phys. Lett. 379 (2003) 230–235.
- [32] Z.L. Jin, X.J. Zhang, G.X. Lu, S.B. Li, J. Mol. Catal. A-Chem. 259 (2006) 275–280.
- [33] Z.P. Yan, X.X. Yu, Y.Y. Zhang, H.X. Jia, Z.J. Sun, P.W. Du, Appl. Catal. B: Environ. 160–161 (2014) 173–178.
- [34] C. Kong, S.X. Min, G.X. Lu, ACS Catal. 4 (2014) 2763–2769.
- [35] W. Zhang, Y. Li, X. Zeng, S. Peng, Sci. Rep. 5 (2015) 10589–10601.
- [36] X.L. Liu, R. Wang, M.Y. Zhang, Y.P. Yuan, C. Xue, APL Mater. 3 (2015) 104403–104408.
- [37] S.Q. Peng, X.P. Zeng, Y.S. Li, Int. J. Hydrogen Energy 40 (2015) 6038–6049.
- [38] W. Zhang, R. Xu, Int. J. Hydrogen Energy 37 (2012) 17899–17909.
- [39] D.D. Liu, Z.L. Jin, Y.K. Zhang, G.R. Wang, B.Z. Ma, J. Colloid Interface Sci. 529 (2018) 44–52.

- [40] Y.B. Li, Z.L. Jin, H.Y. Wang, Y.P. Zhang, H. Liu, *J. Colloid Interface Sci.* 537 (2019) 629–639.
- [41] Y. Wang, B. Kong, D.Y. Zhao, H.T. Wang, C. Selomulya, *Nano Today* 15 (2017) 26–55.
- [42] S. Cao, C.J. Wang, W.F. Fu, Y. Chen, *ChemSusChem* 10 (2017) 4306–4323.
- [43] R. Wang, X.Y. Dong, J. Du, J.Y. Zhao, S.Q. Zang, *Adv. Mater.* 6 (2017) 1703711–1703720.
- [44] M.M. Wang, M.T. Lin, J.T. Li, L. Huang, Z.C. Zhuang, C. Lin, L. Zhou, L.Q. Mai, *Chem. Commun.* 53 (2017) 8372–8375.
- [45] Y. Pan, K.A. Sun, S.J. Liu, X. Cao, K.L. Wu, W.C. Cheong, Z. Chen, Y. Wang, Y. Li, Y.Q. Liu, D.S. Wang, Q. Peng, C. Chen, Y.D. Li, *J. Am. Chem. Soc.* 140 (2018) 2610–2618.
- [46] S.H. Liu, Z.Y. Wang, S. Zhou, F.J. Yu, M.Z. Yu, C.Y. Chiang, W.Z. Zhou, J.J. Zhao, J.S. Qiu, *Adv. Mater.* 31 (2017) 1700874–1700883.
- [47] S. Bai, W.J. Yin, L.L. Wang, Z.Q. Li, Y.J. Xiong, *RSC Adv.* 6 (2016) 57446–57463.
- [48] S. Dang, Q.L. Zhu, Q. Xu, *Nat. Rev. Mater.* 3 (2017) 17075–17088.
- [49] B. Liu, H. Shioyama, T. Akita, Q. Xu, *J. Am. Chem. Soc.* 130 (2008) 5390–5391.
- [50] Y.V. Kaneti, J. Tang, R.R. Salunkhe, X.C. Jiang, A.B. Yu, K.C. Wu, Y. Yamauchi, *Adv. Mater.* 29 (2017) 1604898–1604910.
- [51] N.Y. Cheng, L. Ren, X. Xu, Y. Du, S.X. Dou, *Adv. Energy Mater.* 8 (2018) 1801257–1801277.
- [52] Q.L. Zhu, W. Xia, L.R. Zheng, R. Zou, Z. Liu, Q. Xu, *ACS Energy Lett.* 2 (2017) 504–511.
- [53] J.B. Raoof, S.R. Hosseini, R. Ojani, S. Mandegarzad, *Energy* 90 (2015) 1075–1081.
- [54] B. You, N. Jiang, M. Sheng, S. Gul, J. Yano, Y. Sun, *Chem. Mater.* 27 (2015) 7636–7642.
- [55] Y.Z. Chen, C. Wang, Z.Y. Wu, Y. Xiong, Q. Xu, S.H. Yu, H.L. Jiang, *Adv. Mater.* 27 (2015) 5010–5016.
- [56] X. Cao, C. Tan, M. Sindorob, H. Zhang, *Chem. Soc. Rev.* 46 (2017) 2660–2677.
- [57] F. Zou, Y.M. Chen, K.W. Liu, Z.T. Yu, W.F. Liang, S.M. Bhaway, M. Gao, Y. Zhu, *ACS Nano* 10 (2016) 377–386.
- [58] Y. Xu, W.G. Tu, B.W. Zhang, S.M. Yin, Y.Z. Huang, M. Kraft, R. Xu, *Adv. Mater.* 29 (2017) 1605957–1605964.
- [59] Y. Yang, Z.Y. Lun, G.L. Xia, F.C. Zheng, M.N. He, Q.W. Chen, *Energy Environ. Sci.* 8 (2015) 3563–3571.
- [60] L. Hu, R.R. Zhang, L.Z. Wei, F.P. Zhang, Q.W. Chen, *Nanoscale* 7 (2015) 450–454.
- [61] J.L. Long, R. Li, X.L. Gou, *Catal. Commun.* 95 (2017) 31–35.
- [62] J.J. Zhao, X. Quan, S. Chen, Y.M. Liu, H.T. Yu, *ACS Appl. Mater. Interface* 9 (2017) 28685–28694.
- [63] X. Wang, Z.J. Ma, L.L. Chai, L.Q. Xu, Z.Y. Zhu, Y. Hu, J.J. Qian, S.M. Huang, *Carbon* 141 (2019) 643–651.
- [64] Y. Pan, K.A. Sun, S.J. Liu, X. Cao, K.L. Wu, W.C. Cheong, Z. Chen, Y. Wang, Y. Li, Y.Q. Liu, D.S. Wang, Q. Peng, C. Chen, Y.D. Li, *J. Am. Chem. Soc.* 140 (2018) 2610–2618.
- [65] W.L. Gu, L.Y. Hu, J. Li, E. Wang, *ACS Appl. Mater. Interface* 8 (2016) 35281–35288.
- [66] J.X. Xu, J.Y. Gao, C. Wang, Y. Yang, L. Wang, *Appl. Catal. B: Environ.* 219 (2017) 101–108.
- [67] A.D. Giannakoudakis, N.A. Travlou, J. Secor, T.J. Bandosz, *Small* 13 (2017) 1601758–1601766.
- [68] H. Wang, X.Z. Yuan, Y. Wu, G.M. Zeng, X.H. Chen, L.J. Leng, H. Li, *Appl. Catal. B: Environ.* 130 (2015) 445–454.
- [69] X.Y. Li, Y.H. Pi, L.Q. Wu, Q.B. Xia, J.L. Wu, Z. Li, J. Xiao, *Appl. Catal. B: Environ.* 202 (2017) 653–663.
- [70] L. Shi, T. Wang, H.B. Zhang, K. Chang, J.H. Ye, *Adv. Funct. Mater.* 25 (2015) 5360–5367.
- [71] S. Panneri, M. Thomas, P. Ganguly, B.N. Nair, A.P. Mohamed, K.G.K. Warrier, U.S. Hareesh, *Catal. Sci. Technol.* 7 (2017) 2118–2128.
- [72] M. Seredych, S. Los', D.A. Giannakoudakis, E. Rodríguez-Castellun, T.J. Bandosz, *ChemSusChem* 9 (2016) 795–799.
- [73] K.S. Kim, Y. Zhao, H. Jang, S.Y. Lee, J.M. Kim, K.S. Kim, J.H. Ahn, P. Kim, J.Y. Choi, B.H. Hong, *Nature* 457 (2009) 706–710.
- [74] Z. Sun, Z. Yan, J. Yao, E. Beitler, Y. Zhu, J.M. Tour, *Nature* 468 (2010) 549–552.
- [75] M.R. Gholipour, F. Béland, T.O. Do, *ACS Sustain. Chem. Eng.* 5 (2017) 213–220.
- [76] A.L. Luna, E. Novoseltceva, E. Louarn, P. Beaunier, E. Kowalska, B. Ohtani, M.A. Valenzuela, H. Remita, C. Colbeau-Justin, *Appl. Catal. B: Environ.* 191 (2016) 18–28.
- [77] L.L. Bi, X.P. Gao, L.J. Zhang, D.J. Wang, X.X. Zou, T.F. Xie, *ChemSusChem* 11 (2018) 276–284.
- [78] P. Li, H.C. Zeng, *J. Mater. Chem. A* 6 (2018) 2231–2238.
- [79] Y.C. Ge, P. Dong, S.R. Craig, P.M. Ajayan, M.X. Ye, J. Shen, *Adv. Energy Mater.* (2018) 1800484–1800492.
- [80] S.S. Yi, J.M. Yan, B.R. Wulan, S.J. Li, K.H. Liu, Q. Jiang, *Appl. Catal. B: Environ.* 200 (2017) 477–483.
- [81] K.N. Kudin, B. Ozbas, H.C. Schniepp, R.K. Prud'homme, I.A. Aksay, R. Car, *Nano Lett.* 8 (2008) 36–41.
- [82] S.X. Min, G.X. Lu, *J. Phys. Chem. C* 116 (2012) 25415–25424.
- [83] S.X. Min, G.X. Lu, *J. Phys. Chem. C* 115 (2011) 13938–13945.
- [84] Z.X. Qin, Y.B. Chen, Z.X. Huang, J.Z. Su, L.J. Guo, *J. Mater. Chem. A* 5 (2017) 19025–19035.
- [85] X. Li, J.G. Yu, J.X. Low, Y.P. Fang, J. Xiao, X.B. Chen, *J. Mater. Chem. A* 3 (2015) 2485–2534.
- [86] G.J. Ai, H.X. Li, S.P. Liu, R. Mo, J.X. Zhong, *Adv. Funct. Mater.* 25 (2015) 5706–5713.
- [87] L.Q. Yang, J.F. Huang, L. Shi, L.Y. Cao, W. Zhou, K. Chang, X.G. Meng, G.G. Li, Y.N. Jie, J.H. Ye, *Nano Energy* 36 (2017) 331–340.
- [88] X.Q. Hao, Z.L. Jin, H. Yang, G.X. Lu, Y.P. Bi, *Appl. Catal. B: Environ.* 210 (2017) 45–56.
- [89] J.Q. Wen, J. Xie, H.D. Zhang, A.P. Zhang, Y.J. Liu, X.B. Chen, X. Li, *ACS Appl. Mater. Interface* 9 (2017) 14031–14042.